

REPORT DOCUMENTATION PAGE

Form Approved
OMB No. 0704-0188

Public reporting burden for this collection of information is estimated to average 1 hour per response, including the time for reviewing instructions, searching existing data sources, gathering and maintaining the data needed, and completing and reviewing this collection of information. Send comments regarding this burden estimate or any other aspect of this collection of information, including suggestions for reducing this burden to Department of Defense, Washington Headquarters Services, Directorate for Information Operations and Reports (0704-0188), 1215 Jefferson Davis Highway, Suite 1204, Arlington, VA 22202-4302. Respondents should be aware that notwithstanding any other provision of law, no person shall be subject to any penalty for failing to comply with a collection of information if it does not display a currently valid OMB control number. PLEASE DO NOT RETURN YOUR FORM TO THE ABOVE ADDRESS.

1. REPORT DATE (DD-MM-YYYY)		2. REPORT TYPE		3. DATES COVERED (From - To)	
		Technical Paper			
4. TITLE AND SUBTITLE				5a. CONTRACT NUMBER	
				5b. GRANT NUMBER	
				5c. PROGRAM ELEMENT NUMBER	
6. AUTHOR(S)				5d. PROJECT NUMBER <u>2308</u>	
				5e. TASK NUMBER <u>M4S7</u>	
				5f. WORK UNIT NUMBER <u>345382</u>	
7. PERFORMING ORGANIZATION NAME(S) AND ADDRESS(ES)				8. PERFORMING ORGANIZATION REPORT	
		<u>ERC</u>			
9. SPONSORING / MONITORING AGENCY NAME(S) AND ADDRESS(ES)				10. SPONSOR/MONITOR'S ACRONYM(S)	
Air Force Research Laboratory (AFMC) AFRL/PRS 5 Pollux Drive Edwards AFB CA 93524-7048				11. SPONSOR/MONITOR'S NUMBER(S) <u>Please see attached</u>	
12. DISTRIBUTION / AVAILABILITY STATEMENT					
Approved for public release; distribution unlimited.					
13. SUPPLEMENTARY NOTES					
14. ABSTRACT					
<u>20030127 206</u>					
15. SUBJECT TERMS					
16. SECURITY CLASSIFICATION OF:			17. LIMITATION OF ABSTRACT	18. NUMBER OF PAGES	19a. NAME OF RESPONSIBLE PERSON Leilani Richardson
a. REPORT	b. ABSTRACT	c. THIS PAGE	A		19b. TELEPHONE NUMBER (include area code) (661) 275-5015
Unclassified	Unclassified	Unclassified			

MEMORANDUM FOR PRS (Contractor/In-House Publication)

FROM: PROI (STINFO)

14 Oct 99

SUBJECT: Authorization for Release of Technical Information, Control Number: **AFRL-PR-ED-TP-1999-0188**
Greg Spanjers (PRSS) et al., "Preliminary Analysis of Contamination Measurements from the ESEX 26
kW Ammonia Arcjet Flight Experiment"

26th Int'l Electric Propulsion Conference
(Deadline: 19 Oct 99)

(Statement A)

1. This request has been reviewed by the Foreign Disclosure Office for: a.) appropriateness of distribution statement, b.) military/national critical technology, c.) export controls or distribution restrictions, d.) appropriateness for release to a foreign nation, and e.) technical sensitivity and/or economic sensitivity.

Comments: _____

Signature _____ Date _____

2. This request has been reviewed by the Public Affairs Office for: a.) appropriateness for public release and/or b) possible higher headquarters review.

Comments: _____

Signature _____ Date _____

3. This request has been reviewed by the STINFO for: a.) changes if approved as amended, b) appropriateness of references, if applicable; and c.) format and completion of meeting clearance form if required

Comments: _____

Signature _____ Date _____

4. This request has been reviewed by PR for: a.) technical accuracy, b.) appropriateness for audience, c.) appropriateness of distribution statement, d.) technical sensitivity and economic sensitivity, e.) military/national critical technology, and f.) data rights and patentability

Comments: _____

APPROVED/APPROVED AS AMENDED/DISAPPROVED

PHILIP A. KESSEL
Technical Advisor
Space and Missile Propulsion Division

Date

Preliminary Analysis of Contamination Measurements from the ESEX 26 kW Ammonia Arcjet Flight Experiment

G.G. Spanjers*, J.H. Schilling[†], S.F. Engelman[‡], M.J. Dulligan[§], D.R. Bromaghim**
Propulsion Directorate, Air Force Research Laboratory, Edwards AFB, CA

L.K. Johnson^{††}
The Aerospace Corporation, El Segundo, CA

Abstract

The United States Air Force Research Laboratory's Electric Propulsion Space Experiment (ESEX) was launched and operated in early 1999 in order to demonstrate the compatibility and readiness of a 30-kW class ammonia arcjet for satellite propulsion applications. As part of this flight, an array of on-board contamination sensors was used to assess the effect of the arcjet and other environments on the spacecraft. The sensors consisted of microbalances to measure material deposition, radiometers to assess material degradation due to thermal radiation, and solar cell segments to investigate solar array degradation. Over eight firings of the ESEX arcjet (and 33 min. 26 sec operating time), the following preliminary results are reported. The microbalances show no measurable deposition from the arcjet, in agreement with predictions. The radiometer near the thruster, viewing the arcjet plume and body, experiences a change in the thermal properties of its coating from the firings. Radiometers with no view of the arcjet, or a view of only the plume, show no change. During firings, the solar cell segments, near the thruster, show decreasing open-circuit voltage; probably attributable to an additional electrical load provided by the plume plasma. The solar cells also exhibit a 3% decrease in non-firing, solar-illuminated short-circuit current over the eight arcjet firings, attributable to decreased solar transmission of the cover glass. However, no effects associated with the arcjet are observed on the spacecraft solar arrays. These data are in good agreement with model predictions, where available. In general, contamination effects are observed only on sensors near the thruster exhaust nozzle, a location unlikely to be used in an operational high-power electric propulsion system. No contamination effects are observed in the backplane of the thruster. For future programs, while engineering measures may be needed for spacecraft equipment in the immediate vicinity of the thruster body, the arcjet environment is generally benign.

I. Introduction

Operation of thermal control and optical surfaces can be impaired by material deposition on spacecraft surfaces. Excessive heat flux can degrade the emissive and

absorptive properties of spacecraft materials changing the thermal balance of the satellite. Solar cell operation can be degraded by the presence of a conductive plasma exhaust. Understanding the coupling of these effects with high-power electric propulsion is of

* Project Scientist, Member AIAA

[†] Project Engineer, Sparta Inc., Air Force Research Laboratory, Edwards AFB, CA, Member AIAA

[‡] Project Engineer, ERC Inc., Air Force Research Laboratory, Edwards AFB, CA, Member AIAA

[§] Project Engineer, ERC Inc., Air Force Research Laboratory, Edwards AFB, CA, Member AIAA

^{**} Program Manager, Member AIAA

^{††} ESEX Chief Scientist

This paper is declared a work of the U.S. Government and is not subject to copyright protection in the United States

DISTRIBUTION STATEMENT A
Approved for Public Release
Distribution Unlimited

A major goal of the USAF Electric Propulsion Space Experiment (ESEX)¹ is to explore these issues by measuring the contamination effects of a 30-kW class arcjet in flight. ESEX was launched on 23 February 1999 as 1 of 9 experiments aboard the USAF's Advanced Research and Global Observation Satellite (ARGOS)².

An array of sensors is positioned at strategic locations of the ESEX package in order to assess the contamination effects. Mass deposition, which can impact the satellite's optical and thermal control surfaces, is measured using four thermoelectric quartz crystal microbalances (TQCMs). Thermal flux from the arcjet firing is measured using four radiometers. In addition, the radiometers are coated with S13-GLO, a common thermal surface material with low solar absorptivity and high emissivity. Measurement of heat transfer through the coating determines the degradation of S13-GLO when subjected to the spectral emission of the high-power arcjet. This degradation impacts the thermal design of spacecraft using high-power electric propulsion. A sample Gallium Arsenide (GaAs) solar array segment placed near the arcjet nozzle determines the potential for plasma-solar array interactions or obscuration of the solar flux, which can have a deleterious impact on the satellite power generation capability.

During 8 firings of the ESEX arcjet, no measurable material deposition is observed that is attributable to the steady-state operation of the arcjet. The radiometer placed near the thruster exit, with a view of both the arcjet plume and body, shows material degradation of the sensor thermal coating from the arcjet firings. Radiometers with no view of the arcjet, or a view of only the plume, show no measurable degradation. Thermal transient analysis, required to determine the heat flux to the spacecraft from the arcjet firing has not as yet been performed. Solar cell segments placed near the thruster exhaust show increasing degradation through the experiment,

attributable to the exhaust plasma partially shorting the solar cell load. The solar array measurements also show a 3% decrease in power generation over the eight arcjet firings, attributable to degradation in solar transmission through the cover glass material. No contamination effects associated with the arcjet firing are observed on the main ARGOS solar arrays.

These preliminary ESEX contamination results are very promising for the integration of high-power electric propulsion on commercial and government satellites. Although degradation associated with contamination is observed, in each case the effect is observed only on sensors placed very near, and with a direct view, of the exhaust nozzle of the thruster. It is highly unlikely that material or sensors would be located this close to the thrusters exit plane in an operational high-power electric-propulsion system. Contamination sensors located in the backplane of the arcjet show no deleterious effects. For future programs, while engineering measures may be needed for spacecraft equipment in the immediate vicinity of the thruster body, the arcjet environment is generally benign.

II. Contamination Sensors

The ESEX flight unit is equipped with 4 microbalances, 4 Radiometers, and 2 sections of GaAs solar array cells. The sensors are positioned on the ESEX flight unit as shown in Fig. 1, and specific sensor locations are listed in Table 1. In Table 1, angle=0 is defined as horizontal to the thruster exit plane with negative values in the backflow region; and when sensor angle=90 if the sensor normal is directed towards the thruster exit. Several of the critical contamination sensors are visible in the photograph of the ESEX platform in its pre-flight condition, shown in Fig. 2.

A. Thermoelectric Quartz Crystal Microbalances (TQCMs)

As shown in Fig. 1 and Fig. 3, TQCM #1 is positioned on the witness tower, adjacent to radiometer #1 and near the height of the thruster exit plane. TQCM #2 is located on the diagnostic deck below the thermal shield. TQCM #3 is located near the edge of the diagnostic deck and has a view of the arcjet plume. TQCM #4 is mounted on the deployable boom that also contains the EMI antenna. At the beginning of the flight the boom was stowed and TQCM #4 faced the spacecraft surface. On Julian day 68.6, the boom was deployed. TQCM #4 then faced into the velocity vector (RAM direction) of the spacecraft. Boom deployment was verified by a response from the on-board accelerometer,^{1,7} and by a subsequent decrease in the collected mass on TQCM #4 indicative of the atomic oxygen erosion expected for a ram-facing surface.

The TQCM sensor is a piezoelectric quartz crystal, driven by an electronic oscillator attached to two metal plates placed on both sides of the quartz blank. This imposes a time dependant electric field between the plates, which drives an acoustic oscillation in the crystal, at a frequency determined by the total thickness of the crystal plus any mass on the outsides of these electrodes. The frequency of the crystal surface motion decreases as mass is added, providing a highly sensitive measurement of mass collection on the sensor face. The piezoelectric quartz crystal is approximately 0.0168 cm in thickness, with an active area of 0.317 cm², and is gold plated. The four ESEX TQCMs are the MK-10 model from QCM Research and were chosen to be identical to those used on the Midcourse Space Experiment (MSX) Satellite³ launched in 1996. ESEX could thus take advantage of the characterization and calibration work performed by the MSX team prior to flight⁴. The only difference between the TQCMs on MSX and ESEX is that the MSX sensors used a 15 MHz crystal

whereas the ESEX sensors use the 10 MHz crystals.

The 10 MHz crystal sensor has a signal response of 4.49×10^{-9} grams/cm²/Hz. For a hypothetical contaminant density of 1 gm/cm³, this corresponds to a deposition thickness of 0.44 Angstroms/Hz. The sensor measurement uncertainty is 0.2 Hz according to QCM Research,⁵ but 4 Hz according to the characterization performed for MSX.⁴ The higher MSX uncertainty was due to a cyclic variation in the sensor frequency observed during 21-day drift tests. For the ESEX data, the 4 Hz uncertainty is appropriate for long-term measurements of contaminants due to effects such as spacecraft outgassing. The lower 0.2 Hz uncertainty is appropriate for short duration events such as the sensor response to a short (~15 minute) arcjet firing. The frequency response is on the order of microseconds and not an issue for the ESEX measurements.

Exposure of the TQCM crystals to radiation from the sun or the arcjet firing affects the oscillation frequency by creating a temperature gradient across the crystal diameter.^{3,5} Each time the sun comes into the field of view of the QCM, the crystal will reflect some of the radiation, but also partly absorb the radiation, causing a thermal gradient and thus a frequency change. The effect is temporary, with the TQCM returning to the original frequency when the radiation source is removed. From an operations perspective, this *insolation* effect causes the TQCM data to oscillate with the frequency of the orbital cycle, and with amplitude dependent on the solar flux at each sensor. An example is shown in Fig. 4, where the frequency for TQCM #1 is plotted over 2 days. The solar flux causes an oscillation amplitude of about 200 Hz while mass change on the sensor face causes the slow 30 Hz rise observed over the 2 days. The amplitude of the solar oscillation for TQCM sensors 2,3, and 4 is approximately 160 Hz, 130 Hz, and 160 Hz respectively. The frequency change due to

mass deposition can be deconvoluted from the insolation oscillations by either subtracting the solar oscillation effects, or by using data from the same relative time during each orbit. For the initial analysis presented here, we use either the later technique, or simply show the full oscillation.

The TQCMs can be controlled to temperatures between 193K and 353K, strongly dependent on the heat sink temperatures. Pre-flight ESEX thermal analysis indicated that temperatures as low as 173K might be achieved on-orbit for sensors 2 and 3. During the ESEX flight a minimum temperature of 193K was achieved on all 4 sensors, but it could not be maintained through the solar cycle. A 210K temperature was found to be maintainable through the solar cycle. To reduce the potential for temperature oscillations during an arcjet firing, where the TQCM heat sink is subjected to additional thermal flux, the TQCM sensor temperature was adjusted to 218K and maintained through the ESEX experiment. The TQCM sensors are baked-off by increasing the temperature so as to vaporize some of the condensed material. By comparing the temperature at which the deposited mass is reduced to vapor pressure curves of the candidate specie, the composition of the deposited material can be determined. A total of five bake-offs at temperatures of 298K and 322K have been performed to date. At least one more bake-off will be conducted prior to the ESEX contamination sensors being turned off. A thermographic analysis of the bake-off data, to identify the depositing species, has not been performed and will be presented in a later paper.

“Mass deposition” (or loss) measured by the TQCMs can be a result of a many physical processes including condensation, vaporization, absorption, chemical reaction into more/less volatile molecules, energy deposition releasing previously collected material, sputtering, etc. For this preliminary analysis of the flight data we

refer to a change in the TQCM sensor mass as a generic “mass deposition” without attempting to identify a specific physical process for the observed mass increase or loss.

B. Radiometers

The locations of the ESEX radiometers relative to the arcjet nozzle are shown in Fig. 5. Radiometer #1 is located on the diagnostic tower adjacent to TQCM #1, where it has a direct view of the arcjet body and plume. Radiometers #2 and #4 have a view of the arcjet plume, but are blocked from arcjet body emission by the thermal shield. Radiometer #3 on the diagnostic deck has no direct view of either the arcjet body or plume.

These sensors, shown schematically in Fig. 6, consist of titanium witness plates supported by a narrow titanium strut and an insulating nylon bushing. A reflective aluminum housing surrounds the entire assembly except for an aperture on the front face. The temperature of the radiometer sensor and base are measured using thermocouples with an accuracy of $\pm 1^\circ\text{C}$. The temperature measurements are used to calculate the heat flux through the radiometer coating according to

$$Q_{IN} = Q_{RAD} + Q_{I2} + kA \frac{dT}{dx} + mC_p \frac{dT}{dt}$$

Changes to the heat flux through the coating can than be used to infer changes to thermal properties of the coating material.

The radiometer face is coated with S13-GLO white paint with an emissivity of approximately 0.25 in the visible range, increasing to 0.85 in the infrared. This is a commonly used coating for spacecraft thermal control, but is known to degrade due to solar UV and charged particle interactions. The degradation of the coating in response to the emission spectrum of the arcjet is not known but will be explored as part of the ESEX flight experiment.

C. Solar Cells Segments

Possible effects of arcjet operation on solar array performance is a matter of understandable concern. To address this issue, two small solar array segments are mounted on top of the ESEX diagnostic tower as shown in Fig. 5. Each segment consists of four gallium arsenide cells in series, under a cerium-doped borosilicate cover glass. The arrays are mounted at a 45-degree angle to allow direct exposure to both incident sunlight and to the arcjet body and plume. One solar array is connected to an open-circuit voltage sensor, the other to a short-circuit current sensor, allowing independent measurement of both parameters. A thermocouple is mounted to the base of the solar array assembly to monitor solar array temperature with an accuracy of $\pm 1^\circ\text{C}$.

Under direct solar illumination and at temperatures expected for on-orbit operation, the GaAs solar cell arrays produce a current of approximately 212 mA and a voltage over 4 V. Unfortunately, the sensing circuit for the open-circuit voltage cannot read values greater than 4.2 volts, so the data is truncated at that value during periods of direct solar illumination.

III. Flight Data

The ARGOS host spacecraft for ESEX was launched 23 February 1999 from Vandenberg AFB using a Delta II launcher into a 97 degree near-polar orbit at 846 km altitude. The ESEX contamination diagnostics were powered up to receive data 1 hr 25 min after launch. The TQCMs were first commanded to cool on orbit 8 hrs 14 min after launch to enable measurements of the spacecraft outgassing during the vehicle initialization and check-out. A total of 8 ESEX firings were performed between 15 March 1999 and 21 April 1999. Following the 8th firing, a battery anomaly occurred which precluded additional firings. The ESEX events,

including the battery anomaly are described in detail in Ref. 1. A summary of the ESEX events related to the contamination measurements is shown in Table 2.

A. TQCM Measurements

In general, the TQCM data shows three effects in response to arcjet firings. Two of these are apparent in Fig. 7, which shows an expanded view of the TQCM response to Firing 4. In Fig. 7 a sharp frequency decrease of 263 Hz is observed coincident with the arcjet power. For identification purposes this will be referred to as the *temporary* frequency change. Following the firing a smaller *permanent* frequency decrease of 21 Hz is apparent. The third effect is shown in the same plot for TQCM #1, shown on a slightly longer timescale in Fig. 8. Following the firing the TQCM experiences a period of increased mass deposition rate, evinced by the increased slope in the sensor frequency versus time. This increased deposition rate lasts for about 1 day and is accompanied by an increase in the surrounding temperature, as measured at the base of the adjacent radiometer #1 and co-plotted with the TQCM #1 frequency.

Figure 9 shows each of the 4 TQCM response to the 6 arcjet firings with duration greater than 2 minutes. In general, behavior similar to that described above is seen for each firing with 2 exceptions. TQCM #1 (located on the witness tower and viewing the arcjet nozzle) shows a 140 ng/cm^2 jump in mass deposition with the first firing (F-1C, 141 sec.). Since similar jumps are not apparent on the subsequent firings (F-2 through F-6) this jump is attributed uniqueness to the first firing of the arcjet and not an indicator of steady-state operation. TQCM #2, shielded by the arcjet thermal shield shows no permanent frequency decrease from the firings but does exhibit the 1 day period of increased deposition following each firing. The temporary frequency decreases coincident with the arcjet firings are not visible on the longer timebase shown in Fig. 9.

The TQCM mass deposition recorded from shortly after launch through the battery anomaly is shown in Fig. 10. Each of the TQCMs show a rapid rise shortly after launch that decays in time, indicative of a decreasing outgassing rate from the spacecraft. Bake-off events, denoted by the vertical dashed lines, correspond to times when the TQCM sensors are commanded to heat and vaporize off collected mass. Sunsafe modes of the satellite are accompanied by a data drop-out, and typically a decrease in the total mass deposition. The mass decrease is attributable to the TQCM temperature rising with the loss of power during the sunsafe event, resulting in a material bake-off. TQCM #4 starts the flight with a mass deposition rate that is likely the best indicator of the spacecraft cleanliness since the sensor is directed towards the spacecraft surface prior to boom deployment. After boom deployment, when the sensor faces the spacecraft ram direction, the mass deposition decreases, presumably a result of atomic oxygen erosion.

Not surprisingly, the TQCMs show a strong response to the battery anomaly. TQCM #3 exhibits a strong increase in deposition rate. TQCM #1 shows a discreet jump in mass collected through the event. TQCM #2 also shows a dramatic increase in both mass deposition and the deposition rate. Interestingly, TQCM #2 exhibits a higher deposition rate several days in advance of the anomaly and, in retrospect, may have been a precursor to the event.

B. Radiometer Measurements

Figure 11 shows the sensor and base temperatures for radiometer 1 during Firing #4. At eight minutes, Firing #4 was the longest of the ESEX experiment. Figure 11 shows the radiometer temperatures oscillating with the solar cycle as ARGOS orbits. Figure 12 shows the same data on an expanded time base to illustrate the details of the radiometer response to the arcjet

firing. Both the base and sensor temperatures are observed to rise through the firing, never achieving a thermal equilibrium. Other observations, particularly video images⁶ and solar cell measurements (shown below), indicate that radiant emissions from the arcjet remain nearly constant after the first two or three minutes of operation. In addition, the arcjet itself nearly reaches thermal equilibrium in that period.⁷ The lack of thermal equilibrium complicates the heat flux analysis since care must be given to exactly what materials and masses should be included in the specific heat term with the dT/dt dependence. A transient thermal analysis will be performed on the radiometer response to short heat fluxes and will be presented in a future paper.

Figure 13 shows the behavior of the radiometers over a period of several days at three points in the mission – prior to any arcjet firings, after the eight firings totaling approximately thirty minutes of operation, and after the battery anomaly at the end of the ESEX experiment. For radiometer #1, with exposure to the arcjet body and plume, a significant effect is seen. The radiometer base temperature varies from a minimum of 260 ± 2 K in eclipse to 271 ± 2 K in direct sunlight. Prior to arcjet operation, the sensor head shows a broader range of temperatures, from 257 ± 2 K in eclipse to 275 ± 2 K in direct sunlight. The sensor head is radiating heat when in shadow and absorbing heat in sunlight, as expected. Following the arcjet firings, the maximum temperature in direct sunlight increases to 279 ± 1 K. This sensor temperature increase, at the same base temperature, indicates the thermal characteristics of the S13-GLO coating have changed. Using the governing equation for the radiometer, and ignoring the heat capacity term in view of the much longer characteristic time of the solar cycle, the change in heat flux can be calculated. At the time of maximum heat flux (corresponding to the maximum sensor temperature during the solar cycle) the heat flux through the thermal coating is 0.26W

prior to firing the arcjet. Following the arcjet firings, the maximum heat flux increases to 0.35W, which is a 35% increase over the nominal value. Following the battery failure event, another, modest increase in maximum sensor temperature to 280 ± 1 K is observed, with the minimum temperature again unchanged, indicating that the thermal characteristics of the coating have again suffered a small amount of degradation. Radiometers 2, 3, and 4, show no significant changes during the ESEX mission.

C. Solar Cell Segment Measurements

Figure 14 shows the solar cell voltage and current during the six primary arcjet firings. The current rises above zero about two minutes after arcjet start, reaching a nearly constant value in an additional two minutes, and dropping rapidly to zero after arcjet shutdown. This is consistent with illumination of the solar cells by the glowing arcjet body. Solar cell voltage also follows the same general pattern during the three firings, which occurred during eclipse, with the voltage rise occurring slightly earlier, and the post-shutdown drop-off substantially slower, than is observed for the current. Although not apparent in the scale used in Fig. 14, voltage is also observed to drop off very slightly during the near-equilibrium phase of the longer firings, which is expected as the solar cell temperatures increase.

Two other effects are observed during the arcjet firings. During Firing 1 and 2, 20 s after ignition, there is a small voltage spike peaking at about 1 Volt. Also, immediately after shutdown, there is a small instantaneous jump in voltage, after which the voltage trails off as the arcjet cools. The magnitude of this jump increases from approximately 0.2 volts after the first firing to 0.6 volts after the last in the sequence.

Slightly different behavior is seen on the 3 firings which occurred while the solar cells are exposed to indirect sunlight – the

spacecraft being in sun, but the solar cells shadowed by the arcjet heat shield and/or the ESEX package deck. In this geometry, the solar cells receive enough illumination due to sunlight scattered or reflected from other components of the spacecraft to maintain a steady-state open circuit voltage of 2-3 volts, but no measurable current. The Day 82 firing occurred less than two minutes after the solar cells went into shadow. Solar cell current during these firings followed the same pattern as with the eclipse firings. So did solar cell voltage after the first two minutes of the firing, with the obvious exception of falling off to the original steady-state voltage due to indirect illumination, rather than to zero, after shutdown. The instantaneous post-shutdown jump is observed in these firings, again increasing in magnitude with each successive firing.

The substantial difference between the indirect-illumination firings and the eclipse firings is in the behavior of the solar cell voltage during the first two minutes. In all three cases, the voltage begins to fall off from the original steady-state value about forty seconds into the firing, and drops precipitously at about sixty seconds. Voltage recovers equally rapidly about ten to twenty seconds later, shortly before the current rise and at approximately the time the voltage is observed to rise from zero in the eclipse firings. Both the magnitude and duration of the voltage transient increase in successive firings.

In light of the observed effect of arcjet operation on solar cell voltage, it may be instructive to examine the V-I curve for the solar cells with the arcjet in both on and off states. The illumination of the solar cells by the incandescent arcjet body, which continues for some time following arcjet shutdown, offers an opportunity for such a comparison, and Figure 15 shows voltage vs. current data for all six full-length arcjet firings. With the arcjet shut down, the data falls on a single curve, and even very small currents correlate with open-circuit voltages

in excess of 3 volts. When the arcjet is operating, however, the V-I curve is shifted down in voltage from the arcjet-off case, with the magnitude increasing at each firing. The shift is most pronounced for low current values, and much less significant at currents of 10 mA or greater. This is consistent with the observed voltage jump following arcjet cutoff, and may help explain the voltage drop at sixty seconds after ignition in the partial-illumination cases.

Long-term degradation of the solar cells is shown in Fig. 16 where the solar cell current is plotted over several days at three sample times during the flight; before the arcjet is fired, after the arcjet firings, and after the battery anomaly. Prior to the arcjet firings a solar cell current of about 214 mA is observed. After the eight firings the current drops to about 207 mA. Following the battery anomaly a smaller decrease to about 210 mA is observed. This indicates that during the arcjet firings a 3% decrease in solar cell current and power occurs. The source of this decrease is likely a decrease in the solar transmissivity of the solar cell cover glass. No degradation of the main ARGOS arrays was reported as a result of the ESEX arcjet firings.

IV. Discussion

With each firing (except Firing #1 on TQCM#1) TQCMs #1, 3, 4 show a pronounced decrease in mass deposition, whereas obscured sensor #2 shows no effect. Following the firing, each sensor exhibits a period of increased mass deposition rate. By examining possible sources for the frequency changes, and the expected magnitude of the changes at each sensor, the cause of various TQCM effects can be postulated. Candidate influences that can affect the sensor frequency (other than mass deposition) are a local temperature rise, radiative impingement from the plume, atomic oxygen erosion, and the expulsion of reactive species that act to remove deposited mass.

The influence of a local temperature rise acts to increase the mass deposition rate by increasing the local outgassing rate. A similar effect is observed when the TQCM temperature is changed. When the TQCM sensor is cooled, heat rejection heats the surrounding area, and a period of increased mass deposition rate is observed until thermal equilibrium is reached. Following each firing ESEX temperatures are elevated for about 1 day. This effect is believed to be the source of the increased mass deposition rate following the firing shown in Fig. 7. The elevated ESEX temperatures are apparent in the radiometer #1 base temperature shown in the same figure.

For radiative impingement, one would expect the effect to scale with distance squared from the thruster exit. Figure 17A shows the temporary frequency change, versus distance from the arcjet nozzle, associated with Firing #4 for each TQCM. Also shown is a $1/r^2$ curve expected for frequency changes attributable to radiative impingement from the arcjet. The curve is forced to go through the data point for TQCM #1. The $1/r^2$ fit agrees with the data for TQCM #4. TQCM #2 is well below the curve in magnitude, as expected since the thermal shield blocks the sensor's view of the arcjet body and plume. TQCM#3 is slightly below the curve, however this might be expected since the thermal shield blocks the TQCM#3 view of the arcjet body thus decreasing the radiative intensity at the sensor. Based on this data, the temporary frequency change that is observed during each firing is believed to be a result of radiative impingement from the arcjet plume and body.

The permanent frequency change observed during Firing #4 is shown in Fig. 17B. Clearly a radiative model won't fit this data since TQCM#3 and #4 show effects similar in magnitude to #1. Thermal effects won't fit since #2 experiences a local temperature increase about equal to the other sensors, but shows minimal frequency change. For

interaction with expelled reactive species, one would expect the frequency change to be proportional to the local density, which can be estimated through Direct Simulation Monte Carlo (DSMC) simulations. Shown in Fig. 17B are predictions from a cold-flow DSMC analysis⁸ and a DSMC analysis which includes the arcjet firing.⁹ Both DSMC plots are forced through the data point for TQCM#4. The DSMC analysis shows the decreased response for TQCM#2 relative to TQCMs #1 and #4 in agreement with the data. Contrary to the models, TQCM#1 shows a response about ten times below that predicted by DSMC analysis. Clearly, none of the three influences can be used alone to explain the permanent frequency change observed after each firing. It is presumed that a combination of thermal, radiative impingement, reactive species, atomic oxygen and other effects acting in concert to achieve the frequency changes observed experimentally.

Degradation in the solar cell voltage is believed to be a result of the plasma forming an alternate, shorting current path. The effect is observed to increase with successive firings possibly due to insulator erosion at the short increasing the effective area of the plasma current connection site. This effect is believed to be indicative of plasma exhaust impingement on a solar array and should be avoided in a full-scale flight design. The main ARGOS solar arrays, well in the backfield of the arcjet, reported no degradation of power during arcjet firings. This indicates that the problem can be alleviated through appropriate spacecraft design.

V. Summary and Conclusions

A preliminary analysis of the data from the ESEX flight is performed to assess the contamination associated with the use of the 30-kW arcjet. No material deposition is observed for surfaces held at 218K. The thermal heat load from firing the 30-kW thruster does lead to an elevated spacecraft

temperature, which increases the outgassing rate and hence the mass deposition on the sensors. The latter effect can be tempered through improved thermal design.

Radiometer data indicates material degradation of the S13-GLO coating only for the radiometer nearest the arcjet nozzle with a full view of the exhaust plume and the arcjet body. A 35% increase in heat transfer through the coating is observed following the 8 arcjet firings. Radiometers obscured from the arcjet body, with a view of only the plume showed no evidence of surface coating degradation. Due to a lack of thermal equilibrium during the arcjet firings, further transient analysis of radiometers is required to assess the heat flux due to the arcjet firings.

Solar cell segments show a decrease in output voltage when the arcjet is fired, presumably due to the formation of an alternate conducting path through the exhaust plasma. This deleterious effect can be controlled through the judicious placement of the thruster relative to the solar arrays. The solar array segment also shows a 3% decrease in current following the 8 arcjet firings, presumably a result of decreased solar transmission through the cover glass.

In general, deleterious contamination effects were observed only for sensors placed very near the arcjet nozzle – much closer than would be designed on an operational spacecraft. Sensors showed no contamination effects in the thruster backplane. The ESEX data suggests that the contamination associated with the operation of high-power electric propulsion can be controlled through relatively simple design adjustments.

¹ D.R. Bromaghim, et al., "An Overview of the On-Orbit Results from the ESEX Flight Experiment," AIAA paper 99-2706, June 1999.

² B.J. Turner, and F.J. Agardy, "The Advanced Research and Global Observation Satellite

(ARGOS) Program," AIAA paper 94-4580, Sept. 1994.

³ B.E. Wood, et al., "MSX Satellite Flight Measurements of Contamination Deposition on a CQCM and on TQCMs," AIAA paper 97-0841, January 1997.

⁴ R.J. Bryson, et al., "MSX Thermoelectric Quartz Crystal Microbalances – Calibration and Characterization," 1994 SPIE Intl Symposium, Optical Systems Contamination: Effects, Measurements, and Control IV, paper No. 2261-25, San Diego, Ca 1994.

⁵ D.A. Wallace and S.A. Wallace, "QCM Research Operating Manual – Mark 10," QCM Research, Laguna Beach, CA 1996.

⁶ L.K. Johnson et al., "First results from Optical Diagnostics Applied to the Air Force Electric Propulsion Space Experiment (ESEX)," AIAA paper 99-2710, June 1999.

⁷ J.M. Fife, "Preliminary Orbital Performance Analysis of the Air Force Electric Propulsion Space Experiment (ESEX)," AIAA paper 99-2707, June 1999.

⁸ I. D. Boyd et al., "Modeling the Plume Contamination and Emissions of an Ammonia Arcjet," AIAA-98-3505, 1998.

⁹ M.M. Kriebel and N.J. Stevens, "ESEX Diagnostic Package," TRW Internal Report. 1992.

Table 1: Locations of Contamination Sensors Relative to Arcjet Exhaust Plane

	Distance (cm)	Angle (degrees)	Sensor Angle (degrees)	
Solar Cells	43	3	42	
TQCM 1	40	-11	79	
TQCM 2	45	-60	60	Under radiation shield
TQCM 3	59	-40	40	
TQCM 4	93	-19	19	On deployable boom
Radiometer 1	40	-11	79	
Radiometer 2	48	-37	53	
Radiometer 3	45	-60	60	
Radiometer 4	60	-41	41	

Table 2: Contamination Events during ESEX Flight Experiment

Firing (F) or Event	Date/Time (Zulu)	Julian Date	Duration
Boom Deployed	09MAR99 14:59:57	68.62497	
F-1C	15MAR99 21:55:55	74.91383	2 m, 21 s
F-2	19MAR99 22:32:23	78.93916	5 m, 1 s
F-3	21MAR99 12:24:41	80.51714	5 m, 33 s
F-4	23MAR99 21:27:57	82.89441	8 m, 2 s
F-5	26MAR99 12:45:25	85.53154	6 m, 4 s
F-6	31MAR99 13:05:37	90.54557	4 m, 29 s
F-7	02APR99 22:09:03	92.92295	53 s 38 s
F-8	21APR99 12:22:12	111.51542	42 s
Battery Anomaly	22APR99 15:18:37	112.63793	

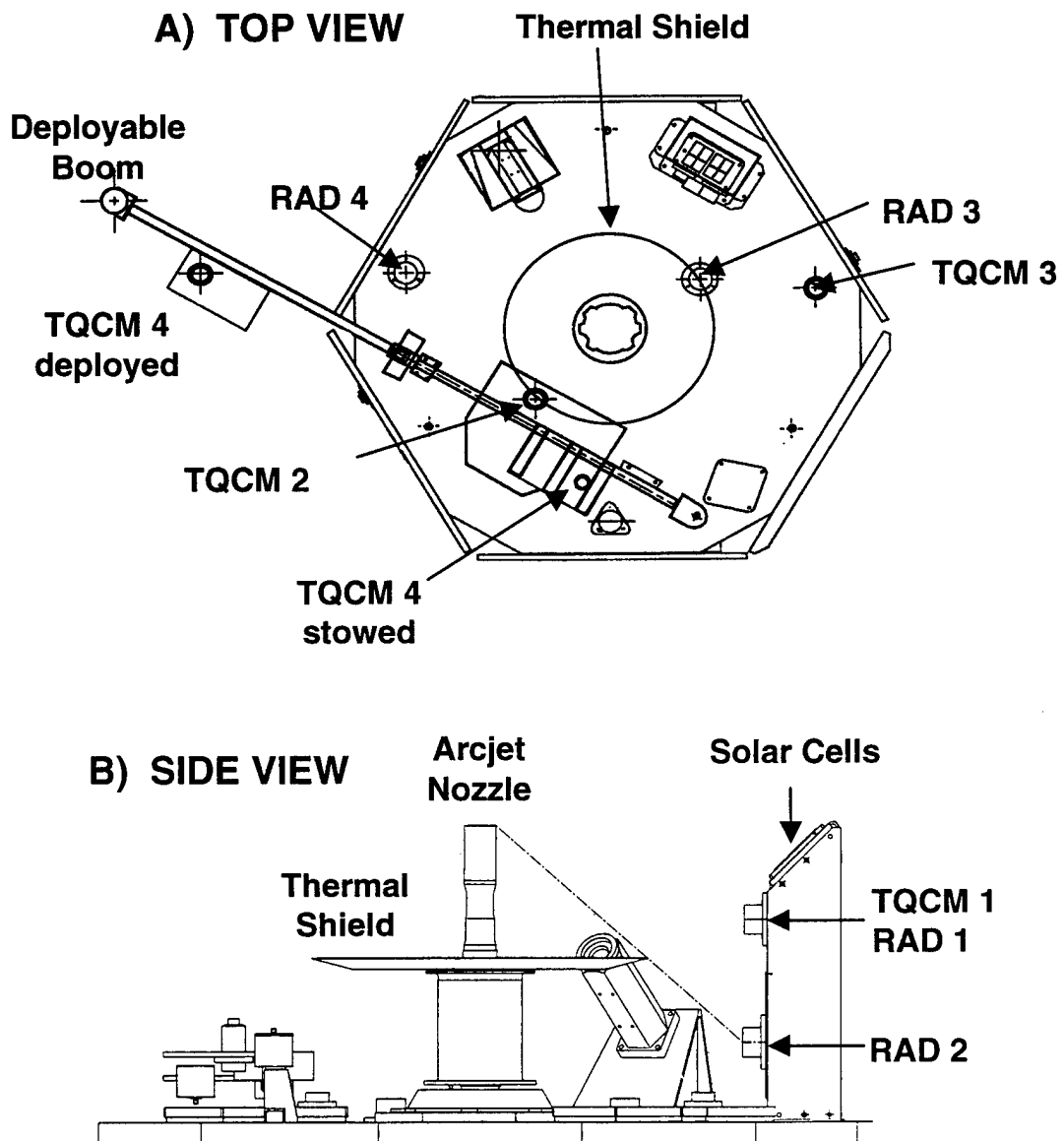


Fig. 1 (A) Top view and (B) Side view of ESEX showing the locations of the contamination sensors.

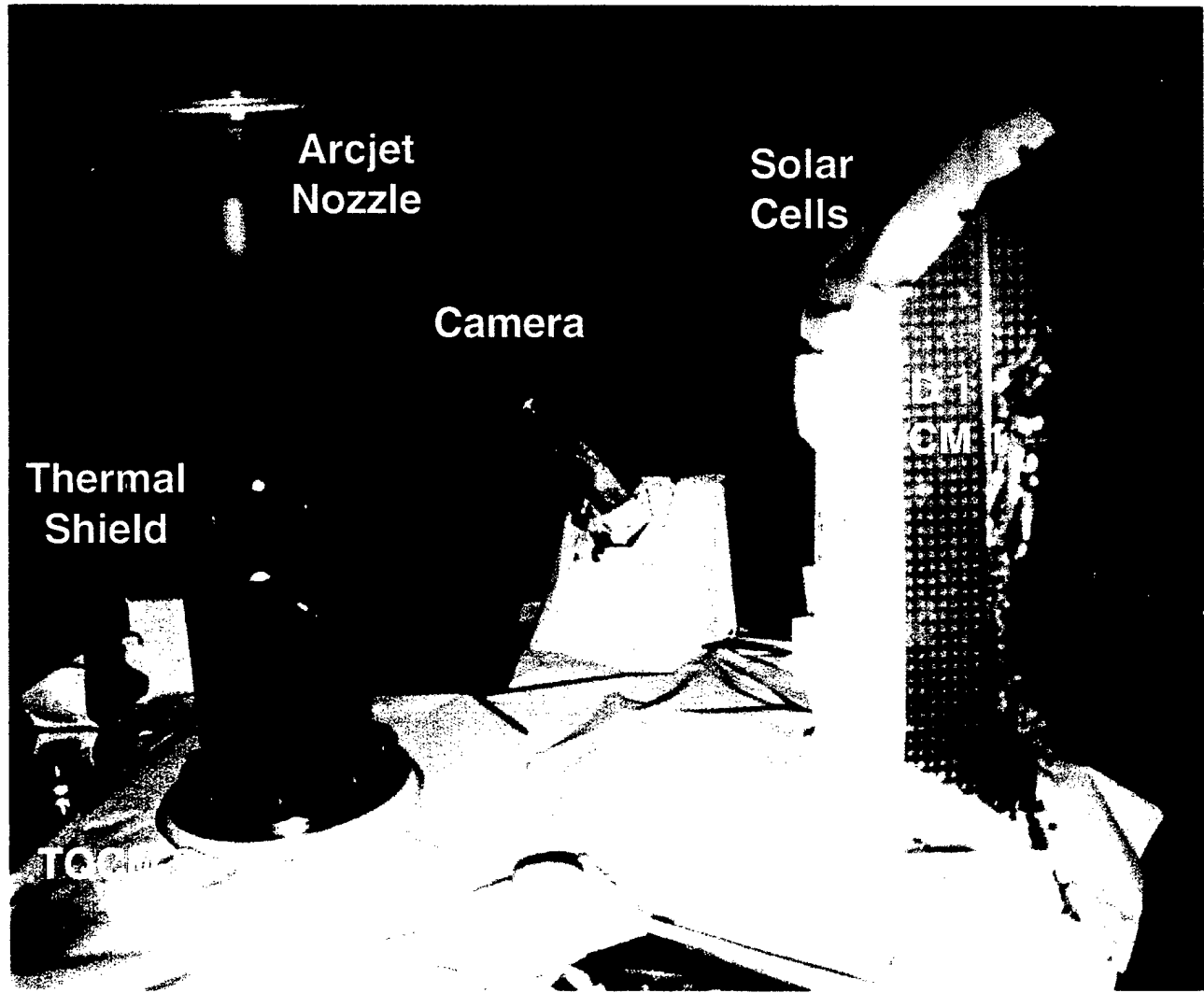


Fig. 2 Photograph of the ESEX platform in its pre-flight condition

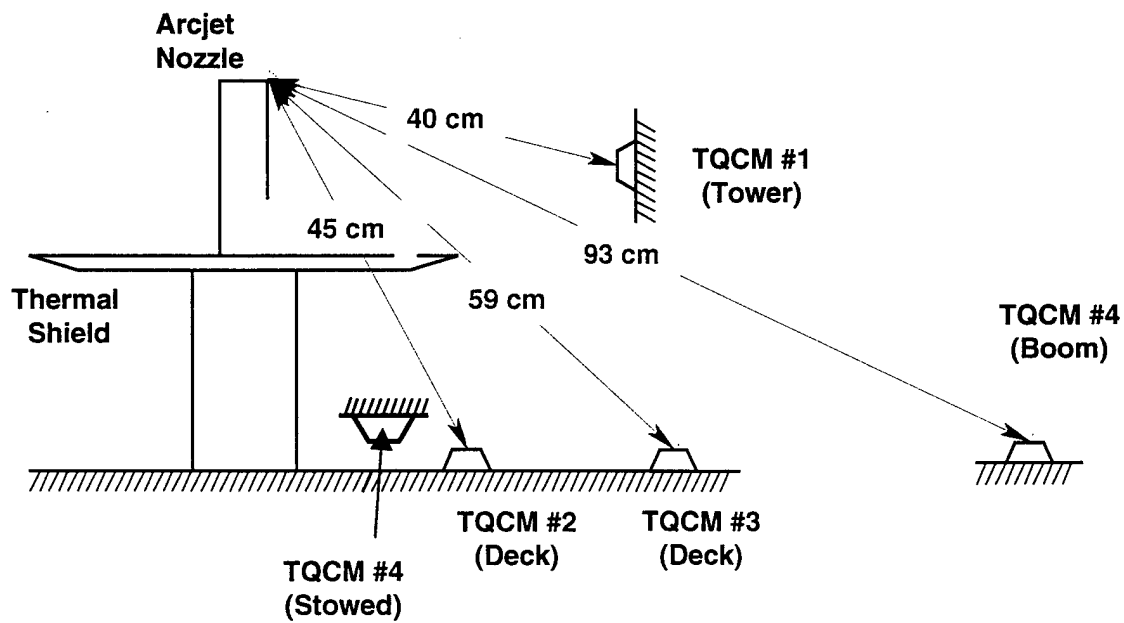


Fig. 3 TQCM Locations relative to the arcjet nozzle. TQCM 4 is in the deployed position for all of the arcjet firings.

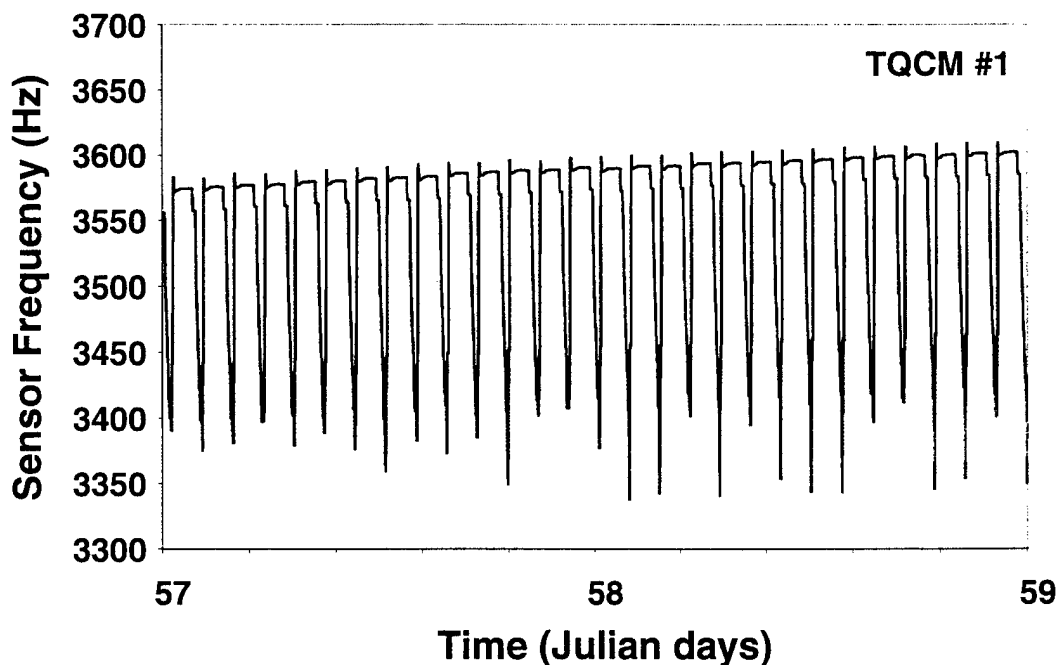


Fig. 4 Representative TQCM data showing the slow frequency increase due to mass deposition superimposed on the larger solar cycle.

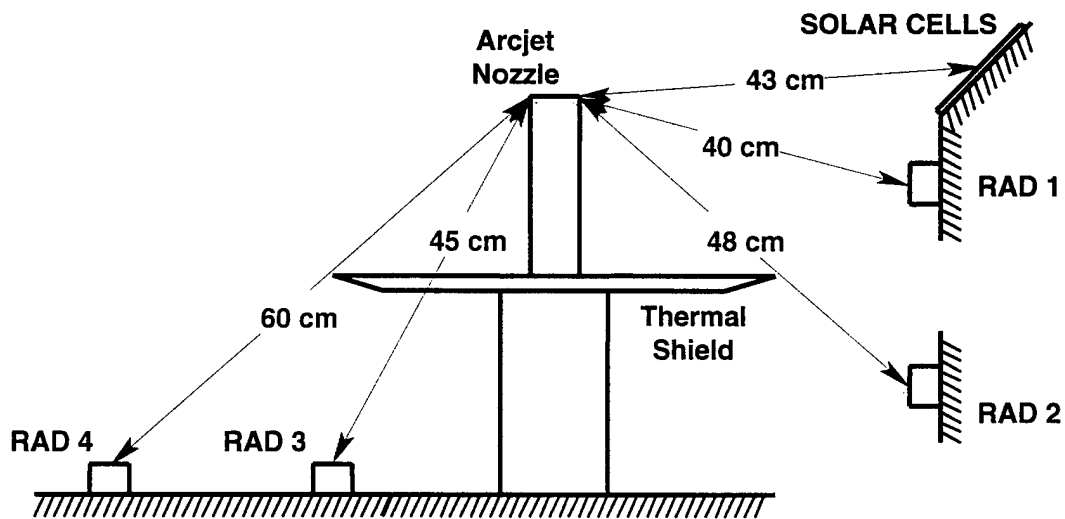


Fig. 5 Positions of the 4 Radiometers and the Solar Cell segment in relation to the arcjet nozzle.

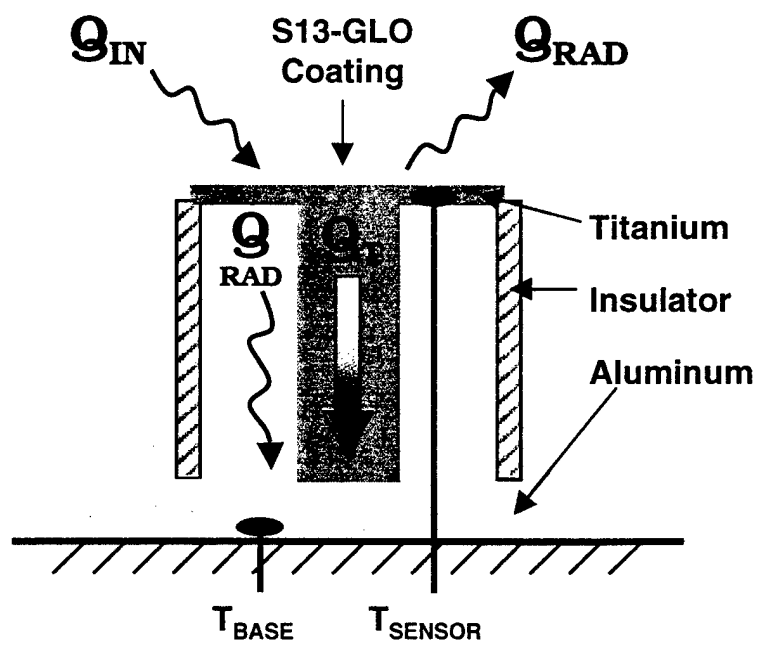


Fig. 6 Schematic diagram of the ESEX radiometer sensors to measure heat flux and material degradation of the S13-GLO thermal coating. The radiometer base is 2.9" in diameter.

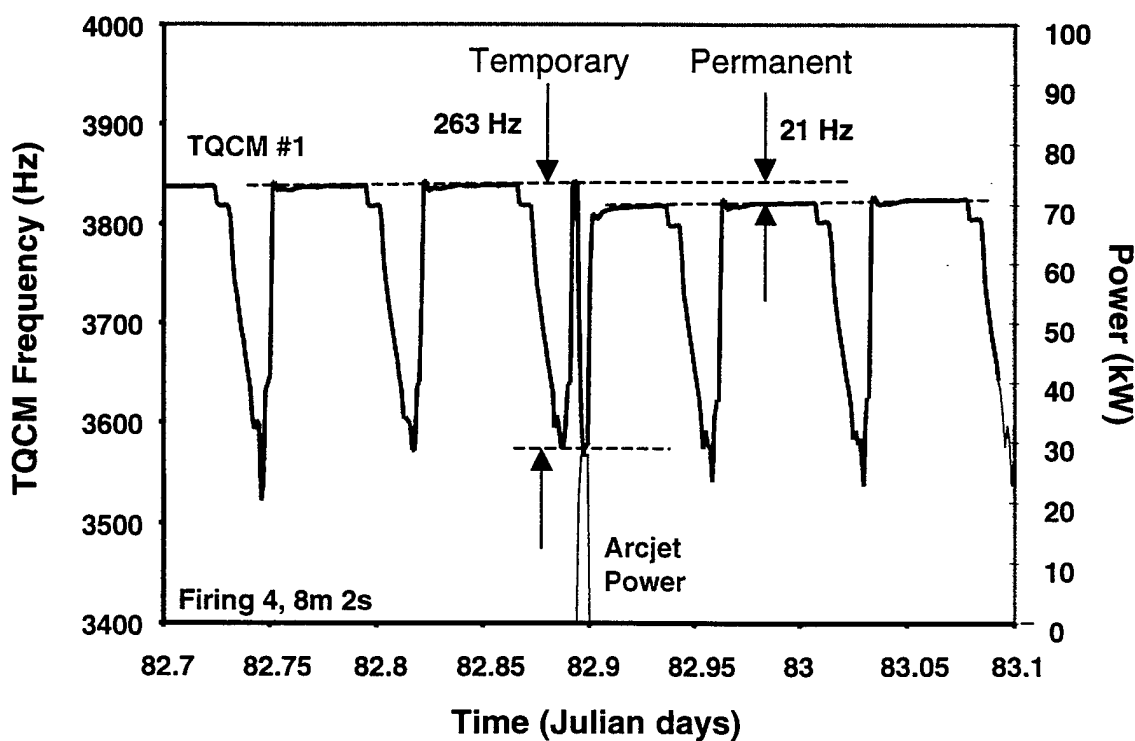


Fig. 7 Typical TQCM response to an arcjet firing. Shown is the output frequency from TQCM #1 during Firing 4.

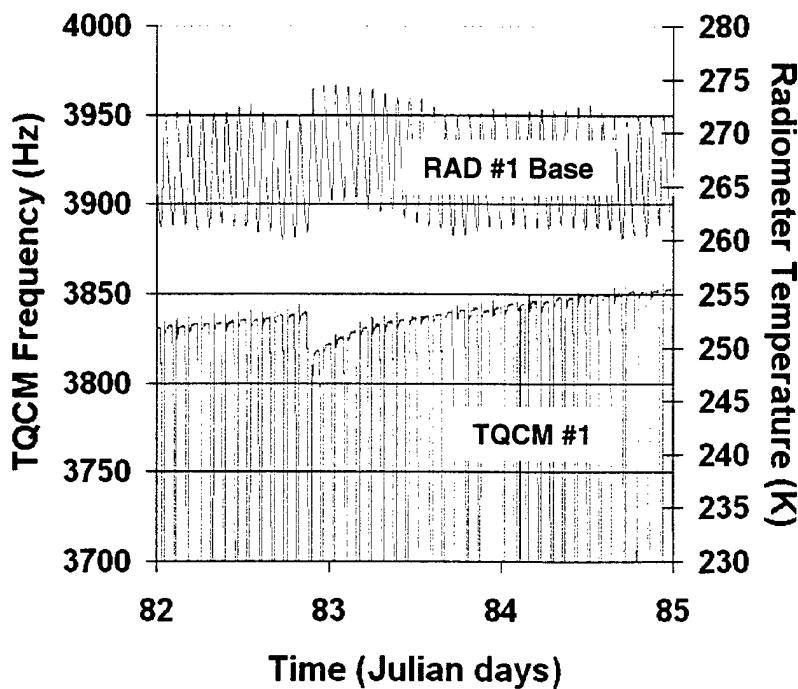


Fig. 8 TQCM#1 response to Firing #4 shown with a longer time base. Also shown is the local spacecraft temperature measured at the base of the adjacent radiometer #1.

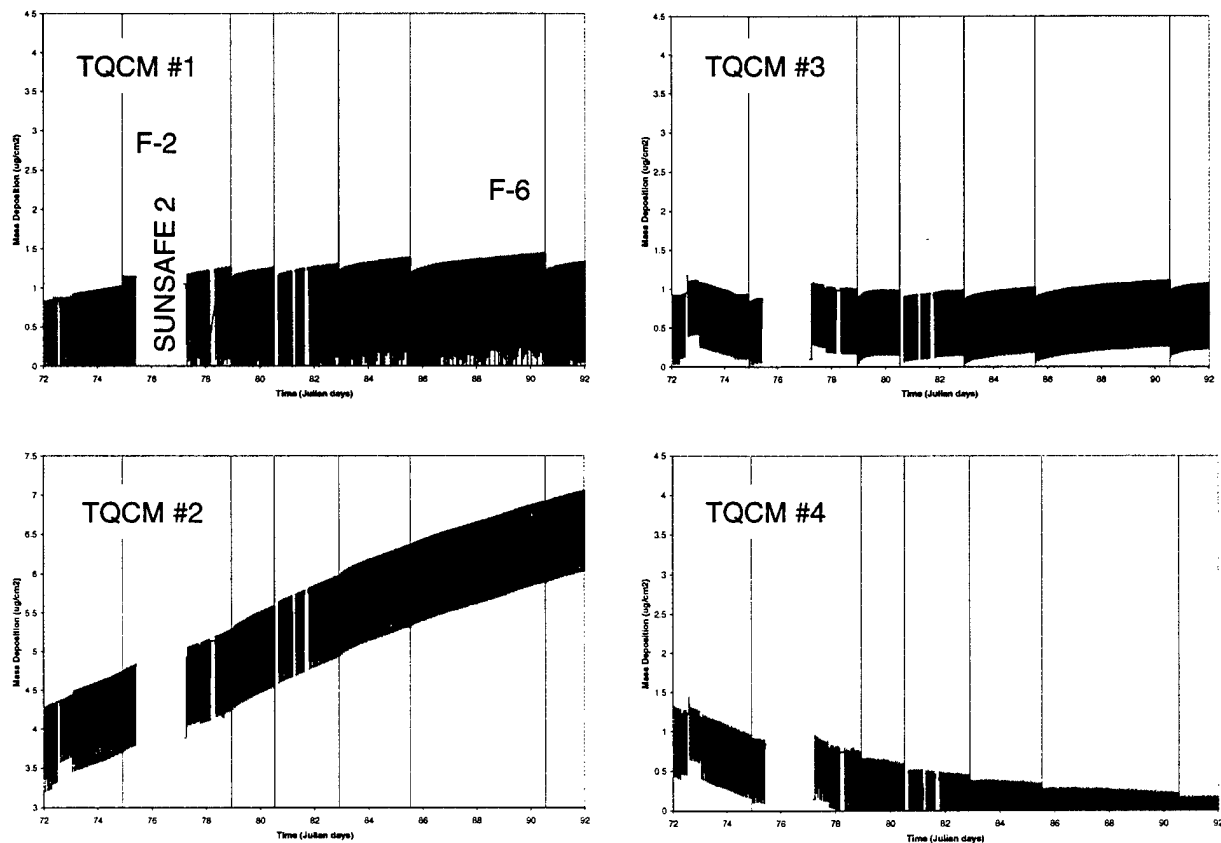


Fig. 9 Mass deposition measured on each of the 4 TQCMs through the primary 6 ESEX firings.

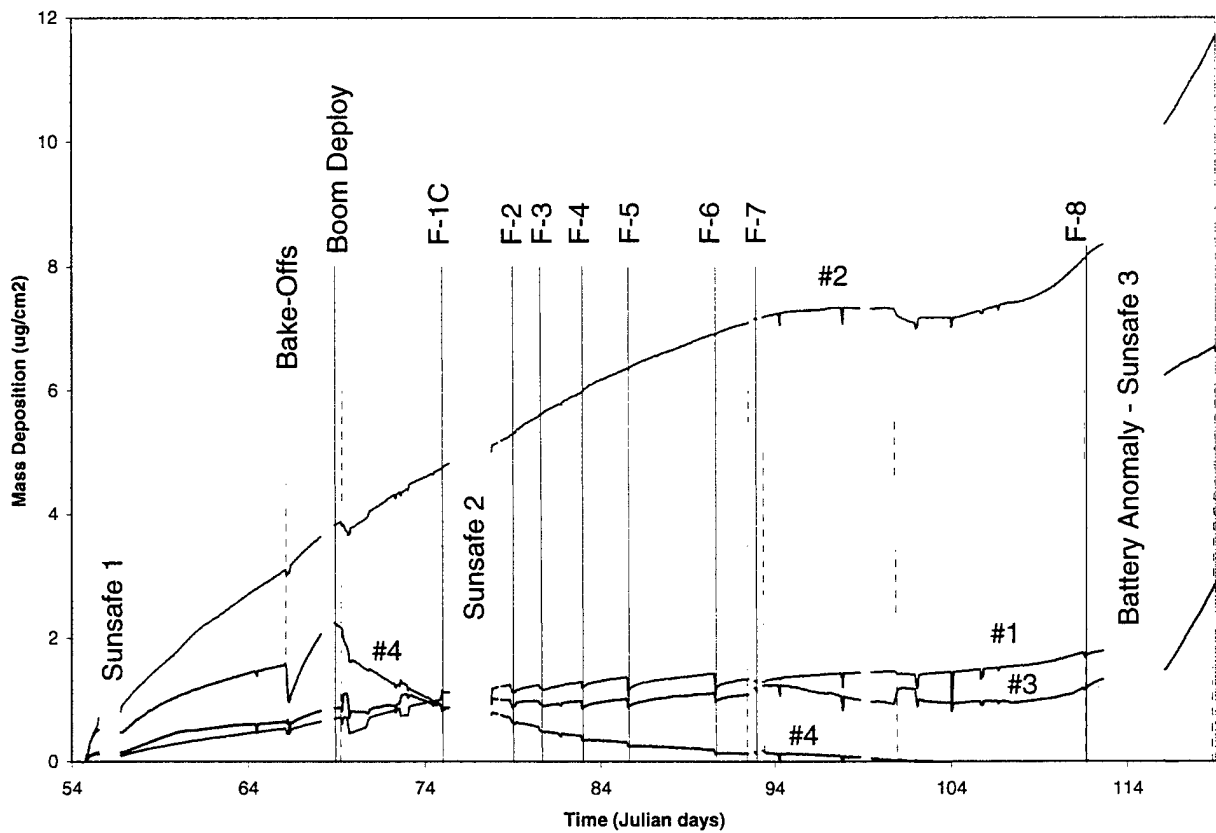


Fig. 10 TQCM behavior from launch through the battery anomaly.

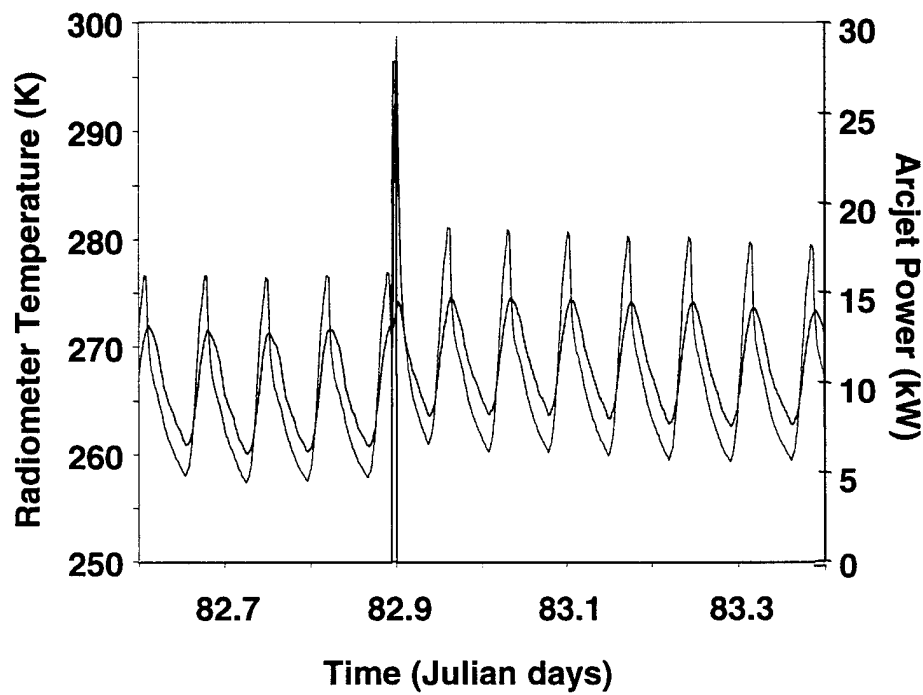


Fig. 11 Mass deposition measured on each of the 4 TQCMs through the primary 6 ESEX firings.

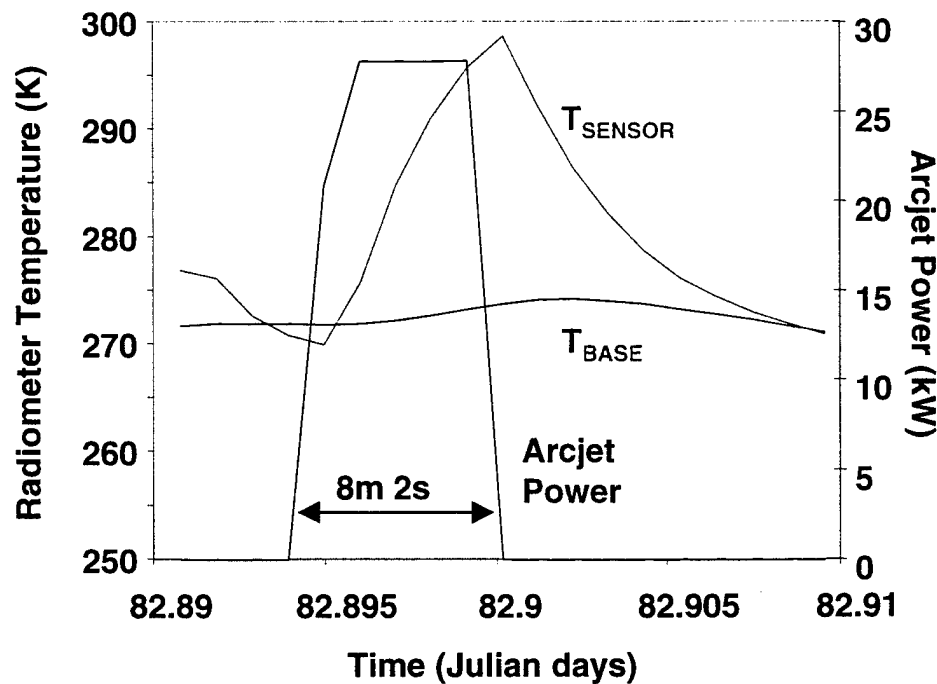


Fig. 12 Mass deposition measured on each of the 4 TQCMs through the primary 6 ESEX firings.

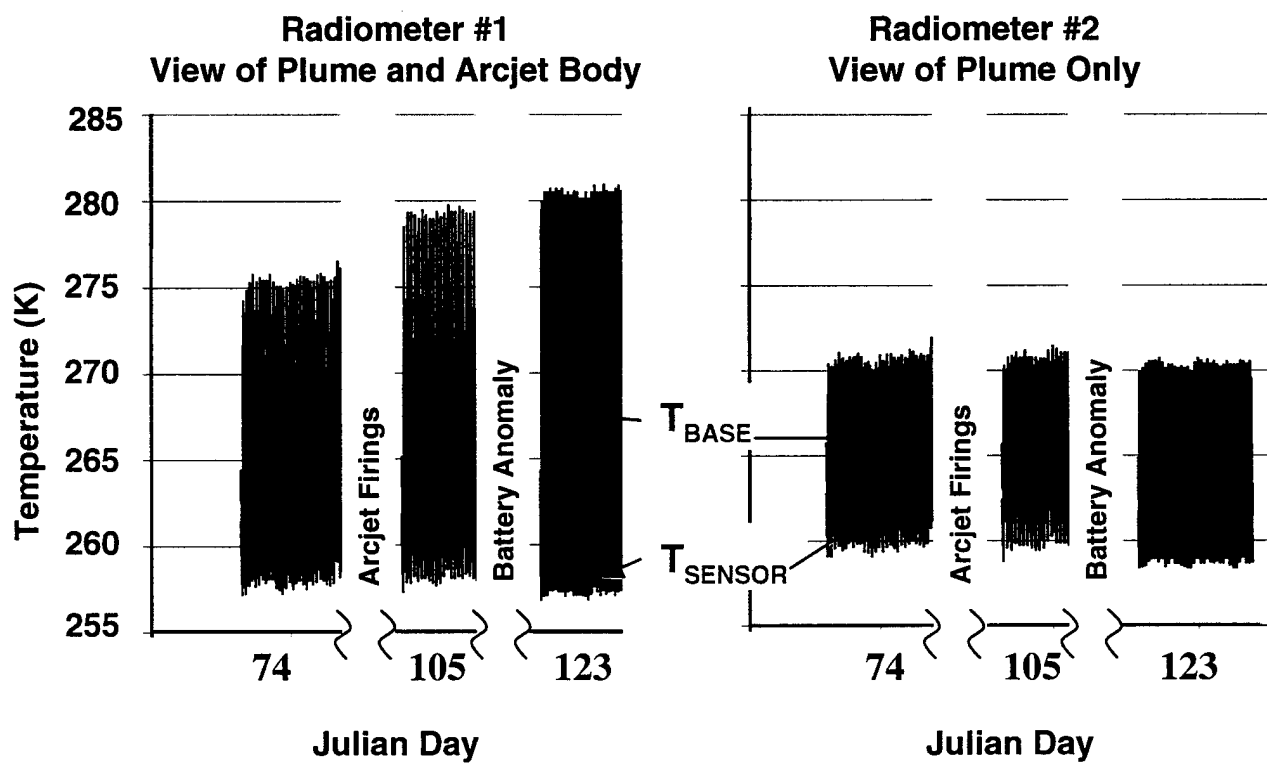


Fig. 13 Mass deposition measured on each of the 4 TQCMs through the primary 6 ESEX firings.

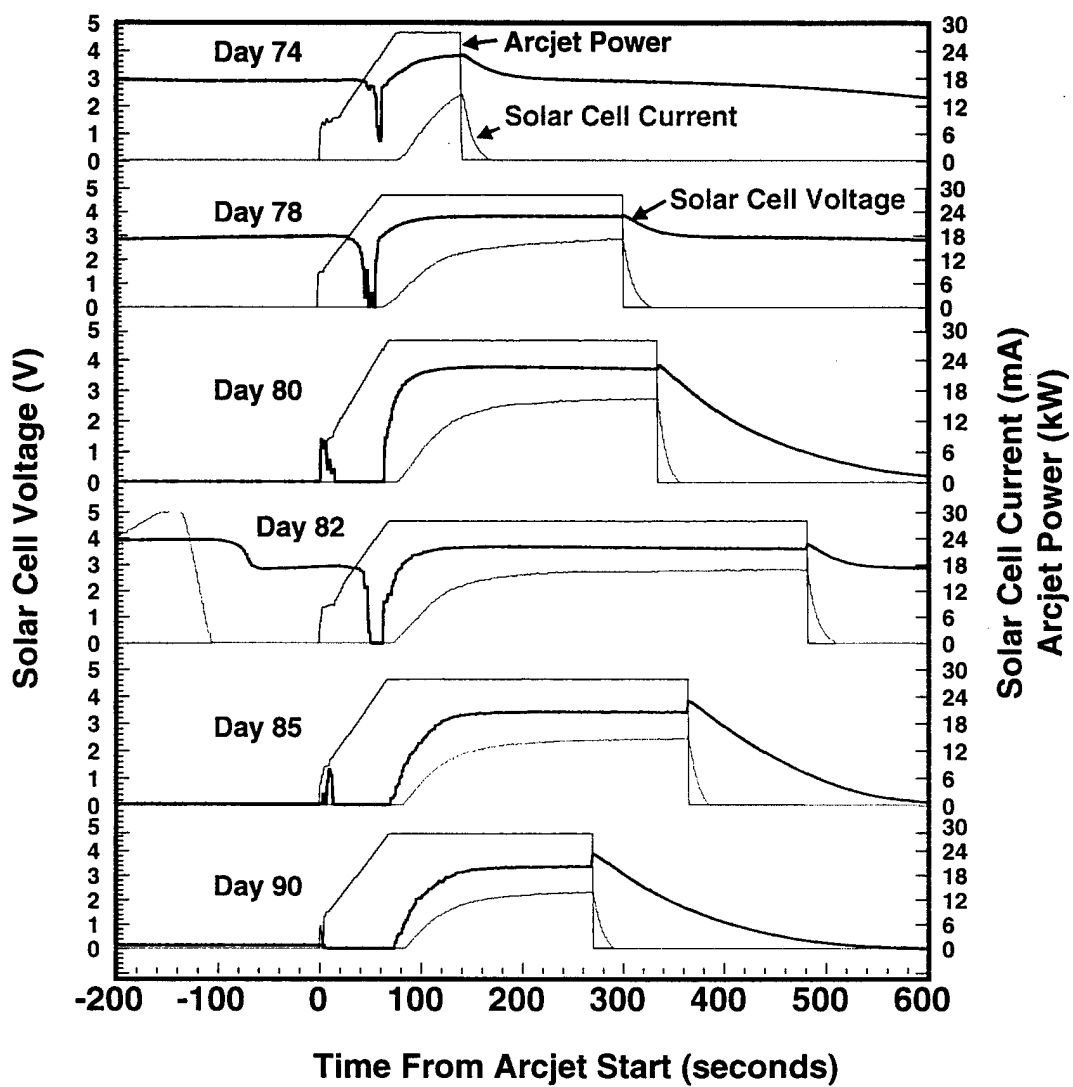


Fig. 14 Solar Cell response to the 6 primary ESEX firings

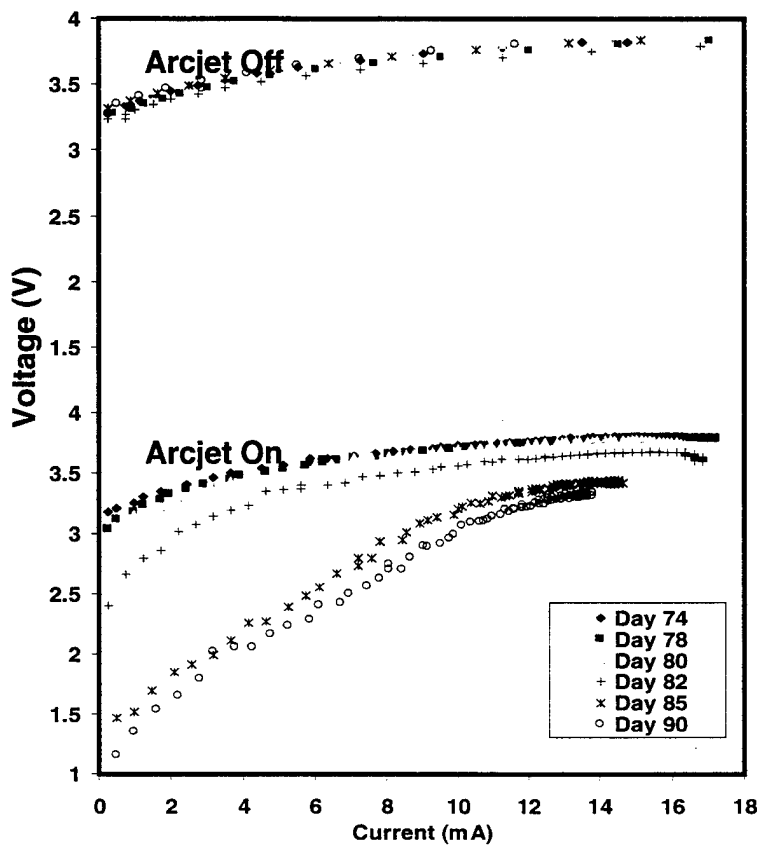


Fig. 15 Solar Cell IV curves during the ESEX firings

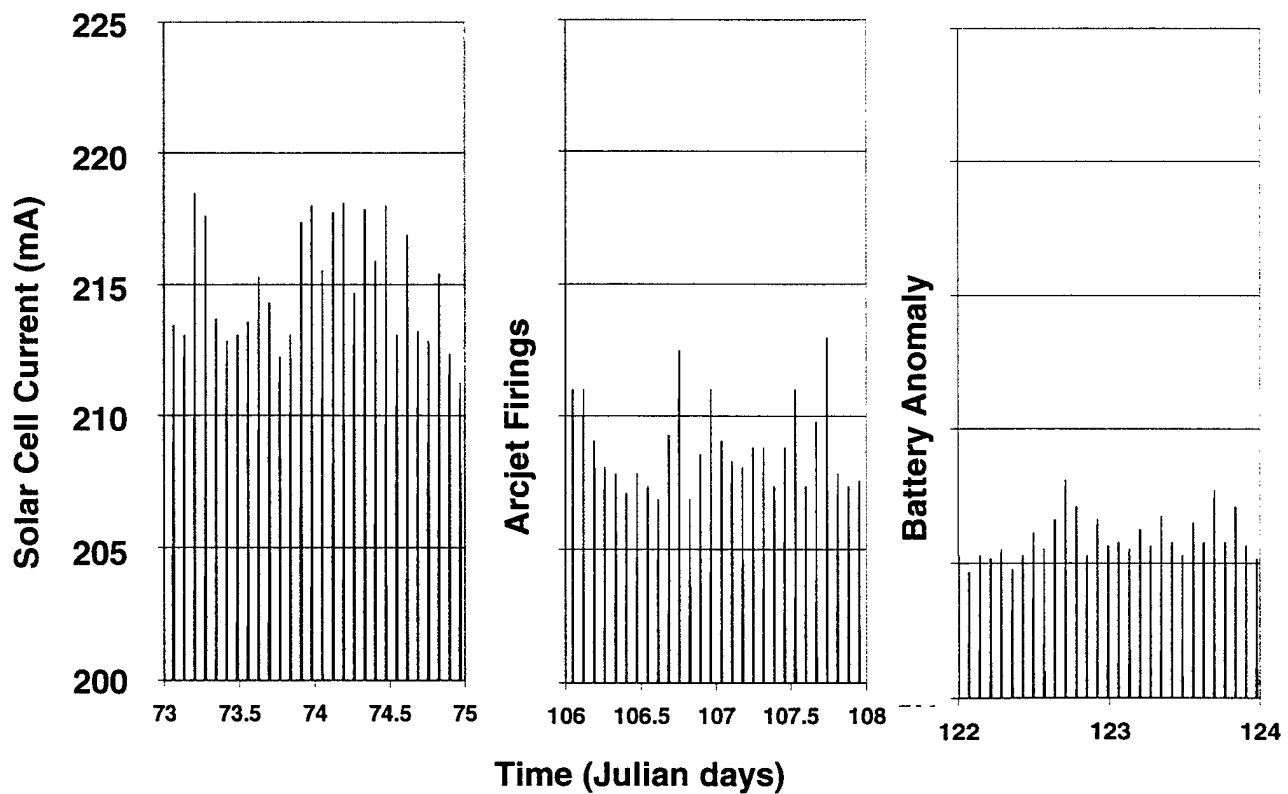


Fig. 16 Solar Cell current at selected times during the ESEX flight